A Decade of Variability on Jakobshavn Isbrae: Ocean Temperatures Pace Speed Through Influence on Mélange Rigidity

Ian Joughin[1], David E. Shean[2], Benjamin E. Smith[1], Dana Floricioiu[3]

5   [1]Applied Physics Laboratory, University of Washington, Seattle, 98105, USA
[2]Department of Civil and Environmental Engineering, University of Washington, Seattle, 98185, USA
[3]German Aerospace Center (DLR), Remote Sensing Technology Institute, SAR Signal Processing, Muenchenerstr. 20, 82230 Wessling, Germany

10   [1]Department example, University example, city, postal code, country
[2]Laboratory example, city, postal code, country

Correspondence to: Ian Joughin (ian@apl.washington.edu)

Abstract. The speed of Greenland's fastest glacier, Jakobshavn Isbrae, has varied substantially since its speedup in the late 1990s. Here we present observations of surface velocity, mélange rigidity, and surface elevation to examine its behaviour over

15   the last decade. Consistent with earlier results, we find a pronounced cycle of summer speedup and thinning followed by winter slowdown and thickening. There were extended periods of rigid mélange in the winters of 2016–17 and 2017–18, concurrent with terminus advances ~6 km farther than in the several winters prior. These terminus advances to shallower depths caused slowdowns, leading to substantial thickening, as has been noted elsewhere. The extended periods of rigid mélange coincide well with a period of cooler waters in Disko Bay. Thus, along with the relative timing of the seasonal slowdown, our results

20   suggest that the ocean's dominant influence on Jakobshavn Isbrae is through its effect on winter mélange rigidity, rather than summer submarine melting. The elevation time series also reveals that in summers when the area upstream of the terminus approaches flotation, large surface depressions can form, which eventually become the detachment points for major calving events. It appears that as elevations near flotation, basal crevasses can form, which initiates a necking process that forms the depressions. The elevation data also show that steep cliffs often evolve into short floating extensions, rather than collapsing

25   catastrophically due to brittle failure. Finally, summer 2019 speeds are slightly faster than the prior two summers, leaving it unclear whether the slowdown is ending.

1 Background

Except for a few brief intervals, Jakobshavn Isbrae (see location in Fig. 1) has been the fastest and largest (by discharge volume) glacier in Greenland over the last several decades (Mouginot et al., 2019). In the mid 1990s, it thickened slightly

30   after slowing down relative to the 1980s (Joughin et al., 2004; Thomas et al., 2003). By the late 1990s and early 2000s,

however, it began to speed up as its floating ice tongue disintegrated (Joughin et al., 2004; Krabill et al., 2004; Luckman and Murray, 2005). Although the glacier maintained a steady speed year round in the 1980s (Echelmeyer and Harrison, 1990), following its speedup, a strong seasonal variation in speed developed in response to the annual advance and retreat of its calving terminus (Joughin et al., 2008a; 2008b). The increased extension during the summer speedup produced near-terminus

35 thinning of ~30 m/yr, which was partially offset by ~15 m/yr of thickening as the glacier slowed over the winter (Joughin et al., 2012b). While the speed peaked in the summer of 2012, strong speedups continued over the next several summers (Joughin et al., 2018; 2014). Over the winter of 2016-2017, however, the terminus began to slow (Lemos et al., 2018), leading to a peak speed the summer of 2017 that was comparable to the minimum speeds for several of the previous winters (Joughin et al., 2018).

40

With this slowdown, the terminus region transitioned from ~15 m/yr of net annual thinning to ~15 m/yr of thickening (Khazendar et al., 2019). This slowdown coincided with a period of increased surface mass balance and cooler atmospheric and ocean temperatures (Joughin et al., 2018; Khazendar et al., 2019; Mouginot et al., 2019). While it is clear that seasonal variation modulates Jakobshavn Isbrae's flow speed, the causal links to underlying atmospheric and oceanic forcing remain

45 poorly understood. Here we investigate the nature of the recent changes and investigate potential links to recent climate variability.

While surface velocity is reasonably well sampled over the last decade, past studies have been limited by sparse spatial and temporal sampling of the large and rapid changes in Jakobshavn Isbrae's surface geometry. To help fill this gap, we assembled

50 a substantial collection of digital elevation models (DEMs) from several optical and radar sensors. Together, the velocity and elevation data sets provide a detailed look at the evolution of Jakobshavn Isbrae's terminus region over the last decade.

2 Methods

We used data from a variety of radar and optical sensors to determine surface velocity, elevation, and other conditions in the fjord over the last decade.

55 **2.1 SAR Derived Velocity, Terminus Position, and the Presence of Rigid Mélange**

We determined surface velocity over the fast moving region of Jakobshavn Isbrae for the period from January 2009 through mid-August 2019 by applying standard speckle-tracking methods (Joughin, 2002) to stripmap TerraSAR-X and TanDEM-X synthetic aperture radar (SAR) data provided by the German Aerospace Center (DLR). We also applied these algorithms to several Cosmo-SkyMed images from the summer of 2019, which were provided by the Italian Space Agency (ASI).

60

The formal errors are small (~< 10 m/yr) relative to the speeds we examine here (>1000 m/yr), so the precision is good with respect to points collected using the same imaging geometry and general time period. Because we make the measurements assuming the flow is parallel to the surface (Joughin et al., 1998), however, errors in the surface slope can introduce absolute errors of ~0.5–3%. With the relatively accurate DEMs we used, the errors should tend toward the low end of this range in most instances. Exceptions may occur where large temporal fluctuations in slope occur near the terminus as discussed below. Although we generally update the DEM annually, large intra-annual changes can introduce geolocation errors so that the correct velocity is reported at the wrong location (~50 m displacement error). These absolute geolocation errors can introduce relative geolocation errors of ~100 m between maps created with substantially differing imaging geometries (e.g., from ascending and descending passes). Thus, location errors can lead to large velocity errors (>100 m/yr) in areas with high strain rates, such that the correct velocity is reported at the wrong location. Given the fast speeds we examine, however, the magnitude of such errors has little impact on the analysis described below.

In addition to the glacial ice, the speckle tracker was also applied to the regions in the fjord where an ice mélange (mixture of sea ice and icebergs) is often present. When the mélange is rigid and moves within the bounds of the tracking algorithm (i.e., at speeds similar to the terminus), a successful velocity estimate is returned. In such cases, the velocity is indicative of rigid mélange that is being pushed down the fjord by the advancing terminus (Joughin et al., 2008b). Absence of an estimate usually indicates non-rigid motion in which there is substantial relative motion within the ~200-m dimensions of the tracking window, yielding little correlation between image patches acquired several days apart. Alternatively, the trackers failure to produce a result could indicate strong rotation or extremely fast rigid translation down the fjord (e.g., large calving event or wind-driven advection) at rates beyond what tracker was designed to accommodate (i.e., much faster than the terminus). For the remainder of the text, when we refer to "rigid mélange," we mean a mélange that is being coherently advected at a rate similar to the flow speed at the terminus.

2.2 Terminus Position Data

Using several hundred TerraSAR-X images with ~20-m resolution, we manually digitized the points where the profile shown in Fig. 1 crosses the terminus, as a proxy for the overall terminus position. Because of the rapidly changing elevations relative to the static DEM used for geolocation, the absolute geolocation errors of points at the terminus could be as large as ~100 m. Since we used images acquired from both ascending and descending orbits, the relative error could be nearly twice as large between images, because a given height error will induce geolocation error in opposite directions (i.e., the terminus could appear up to nearly 200 m apart in images acquired at the same time from ascending and descending orbits, even though individually each would be in error by 100 m). Thus, these data are used to examine the overall seasonal pattern of advance and retreat, rather than to identify the calving of individual icebergs, which are typically about 100–200 m in the along-flow dimension (Amundson et al., 2010).

2.3 Terminus Elevation Data

We used elevation data from a number of sources including both optical and radar sensors. All elevations are given as meters
95 above the EGM2008 geoid, which approximates mean sea level. All DEMs were up- or down-sampled to a consistent 25-m
posting for analysis.

We generated DEMs from DigitalGlobe WorldView-1/2/3 (WV) and GeoEye-1 (GE) imagery acquired between June 2008
and May 2015 using the NASA Ames Stereo Pipeline (Beyer et al., 2018) and methods outlined in Shean et al. (2016). The
100 DEMs were co-registered to available ground control points (GCPs from NASA's ICESat, LVIS and ATM lidars) over static
control surfaces (e.g., exposed bedrock) using a rigid-body iterative closest-point algorithm to determine the translation that
minimized the elevation difference between the DEMs and GCPs (Shean et al., 2015). After co-registration, the residual error
of each DEM was estimated using the normalized median absolute deviation (NMAD; Hoehle and Hoehle, 2009) of all GCP-
DEM differences (Shean, 2016), with values for WV DEMs of 0.52 m.
105

We used ArcticDEM strips also derived from WV/GE imagery acquired between 2016–2019 (Porter et al., 2018), generated
using the SETSM processing workflow (Noh and Howat, 2017). The WV/GE DEMs are posted at 2 m, with a swath that is
~13-17 km wide and ~13-110 km long, depending on sensor and acquisition mode. The elevation of each DEM was adjusted
by adding constant to produce a self-consistent set of results that minimized biases in regions of overlap on bedrock. After this
110 procedure, comparison with several thousand independent lidar point measurements yielded a median bias of 1.2 m with
median standard deviation of 0.9 m.

We included DEMs from SAR images acquired between 2011–2013 in bistatic, stripmap mode as part of DLR's TandDEM-
X mission and processed using the Integrated TanDEM-X Processor (ITP) (Rossi et al., 2012). The DEM posting was 5 m
115 with a ~35 km wide and ~50-60 km long footprint. Absolute elevation offsets from baseline-dependent interferometric SAR
(InSAR) height ambiguities were corrected by adjusting the absolute phase offset during InSAR processing. We further
improved the accuracy by applying horizontal and vertical adjustments constrained by ground control points with a similar
procedure to that applied to the WorldView data described above (Shean, 2016), yielding accuracy of 1.2 m.

120 We obtained four DEMs produced by the Glacier and Land Ice Surface Topography Interferometer (GLISTIN) collected in
each spring from 2016 to 2019, which are publicly available from the JPL Uninhabited Aerial Vehicle SAR (UAVSAR)
website (http://uavsar.jpl.nasa.gov). The GLISTIN system uses Ka-Band to limit penetration in ice and has meter-scale
accuracy (Moller et al., 2011), which is comparable to the other DEMs we used.

2.4 Flotation Height

125 We computed the flotation height, h_f, equal to the maximum height that the surface of a column of floating ice could have without its bottom touching the bed, using standard methods and assuming densities of 910 and 1028 kg/m³ for ice and sea water, respectively (Cuffey and Paterson, 2010). The bed data used in this calculation are from BedMachine Version 3 (Morlighem et al., 2017). Estimated bed elevation uncertainty for this region is up to ~100 m, which translates to an uncertainty of 13 m in h_f.

130 ## 3 Results

As described throughout this section, we have assembled a comprehensive set of velocity, elevation, and terminus position data that provide a detailed view of Jakobshavn Isbrae's behaviour over the last decade.

3.1 Velocity and Terminus Position

The top panel in Fig. 2 shows the terminus position (black) along our profile (Fig. 1) as a function of time. Also shown are the
135 points along the profile located 1-km behind the point of maximum annual terminus retreat for each year (T$_{max}$-1km; brown). In determining T$_{max}$-1km for 2014, we excluded two anomalous points associated with rapid retreat and re-advance, which appear to have been from an area that was floating and had little impact on the speed. As in similar time series (Joughin et al., 2014), these data show seasonal variation in terminus extent by more than 2 km, with the terminus retreating farther inland each year through 2012. From 2012 through 2016, the extent of maximum retreat was similar each summer as indicated by the
140 T$_{max}$-1km positions (brown lines Fig. 2). The seasonal transition from advance to retreat typically occurred around March, but it started as early as January (2010) and as late as June (2011). Peak retreat generally occurred in late summer/early fall.

In the winter of 2008–09, a several-kilometre long transient ice tongue advanced, as was the case for the prior winters following the breakup of the more extensive ice tongue (Joughin et al., 2012b). This pattern altered for the 2009-10 through 2015-16
145 winters when there was no substantial ice tongue advance, although, as described below, the terminus was floating at times. The pattern changed again when a floating tongue 4–5 km in length advanced during the winter of 2016–17 (see Fig. 2), with an even longer ice tongue advancing the following winter. A similar ice tongue advanced in the 2018–19 winter, but it was less extensive than those from the prior two winters.

3.2 Mélange Extent

150 We sampled the mélange in a static, 1 km x 1 km region just outside the point of maximum terminus advance for 2010–2019. Because the extent of the floating ice tongue was so much greater in 2009, we moved the sampling region for the 2008–09 winter farther down the fjord (see blue boxes Fig. 1). The blue symbols in the top panel of Fig. 2 indicate the times when rigid

mélange was detected in front of the terminus. This detection of rigid mélange is relatively robust, hence there should be few false detections. Missed detections could result if the speckle-tracker fails due to poor correlation despite the presence of rigid mélange. We examined the individual maps by hand, and there appear to be few, if any, instances of missed detections. As plotted, a gap in coverage would also indicate a lack of mélange. Such gaps are indicated by a corresponding lack of velocity data in the lower panel of Fig. 2 (e.g., gap in Fall 2010).

The duration of periods with rigid mélange varies substantially from year to year. The longest periods of rigid mélange occurred during the 2016–17 through 2018–19 winters, which coincide well with the periods when a more extended floating ice tongue developed. Similarly, there was extensive mélange in the 2008-2009 winter when a floating tongue also advanced (only 2009 is shown in Fig. 2). For other years the mélange generally was less frequent and more sporadic. Mélange was particularly sparse in both 2011 and 2012, which are the years when the greatest retreat occurred. In all summers there was a mélange-free period of at least a few months, which tends to line up well with the periods of summer speedup. In general, extended periods where rigid mélange exists coincide well with periods of terminus advance, which is consistent with similar data from the period from 2005 to 2007 (Joughin et al., 2008b).

3.3 Velocity

The lower portion of Fig. 2 shows the speed at several points along the main trunk, which represents an update to earlier records (Joughin et al., 2014; 2018). For consistency, we use the same locations and naming schemes (M6–M26) as earlier work (Joughin et al., 2008b; 2014). We also include the speed at the point 1-km upstream of the point of maximum annual terminus retreat (T_{max}-1km; see brown Fig. 2 top), which provides speed relative to the evolving terminus position rather than a fixed point. As noted elsewhere (Joughin et al., 2014), when the terminus migrates inland along a reverse bed slope, the speed at a fixed point should increase due both to a thicker calving front and to the reduced proximity to its steep face (Joughin et al., 2014). Thus, the T_{maxn}-1km time series is much faster than the M6 data in the early part of the record when the terminus was more advanced, but the speeds for the two points begin to converge as the terminus migrates inland. From 2012–2016 the speeds at these two points are nearly identical, consistent with their similar proximity to terminus, with separation by ~1-km in the cross-flow direction (see Fig. 1).

Figure 2 indicates that the slowdown that began in the winter of 2016–17 (Joughin et al., 2018; Lemos et al., 2018) continued, with the slowest summer speeds for the 2009–2019 period occurring in 2018. Although the 2018–19 winter speeds were similar to the previous winter, the terminus retreated rapidly beginning in late April with an accompanying increase in speed. By mid-August 2019, the maximum speed was slightly greater than the maximums for the prior two summers. Since the seasonal peak can occur later in the summer or even early fall, further speedup may still occur.

3.4 Elevation

185   We assembled a total of 84 DEMs spanning the period from 2010 to 2019 that incorporates data from ASP- (50) and SETSM-(19) processed WorldView stereo pairs, TanDEM-X acquisitions (11), and GLISTIN (4) airborne campaigns. Figure 2 (top) shows the full time series at points M6 and M9. At these points, surface was highest in late spring 2011 after winter thickening recovered some of the loss that occurred the prior summer. The surface then lowered by ~30 m during the 2011 summer, but thickened moderately (~10 m) during the subsequent winter. As the terminus retreated in summer 2012, the surface at M6

190   dropped by nearly 40 m between June 10 and July 20, coincident with the most extreme speedup event in the entire record. From summer 2012 to summer 2016, there was a fairly consistent annual cycle with the terminus thickening by 35-50 m each winter, and thinning by a similar amount each summer, bringing M6 to near or at flotation in 2013–2015. The record is sparser for 2016, but it is sufficient to indicate that increased thickening occurred during the winter of 2016-17 as the ice tongue advanced and the glacier slowed. As a result, just prior to the summer speedup in 2017, the terminus region was ~35 meter

195   higher than the previous summer (see also Khazendar et al., 2019). Winter thickening continued to outpace summer thinning so that by March 2019, surface elevations near the terminus were only 10 to 20 m lower than those observed during spring of 2011.

Figure 3 shows the surface elevation time series along the profile shown in Fig. 1 along with the flotation height (h_f ; solid

200   grey) computed using BedMachine v3 data (Fig. S1; Morlighem et al., 2017). For reference, the first profile (August 12, 2010) is plotted (black circles) for comparison with each year. The plot for 2018 also includes 3 March 2019 profiles that are nearly identical to the August 2010 profile, indicating some degree of recovery in response to recent slowdown and thickening (Joughin et al., 2018; Khazendar et al., 2019).

205   The data reveal a variety of terminus geometries. Several of the profiles in Fig. 3 show a relatively steep calving face in mid to late summer (e.g., August 17, 2010). Another common configuration involves the area ~0.5–2km upstream of the terminus floating, with elevation well below h_f. At times when the terminus was afloat, there were cases when the elevation tapered smoothly to the water surface with little or no terminal cliff (e.g., August 12, 2010). In many other cases, particularly in many of the early spring profiles, the downstream part of the floating region was relatively flat with a relatively steep calving front.

210

Between 2012 and 2015 in late summer there were often ~1–2 km transverse width depressions with surface heights tens of meters below flotation a kilometre or more upstream of the well-grounded terminus. There are insufficient data to determine whether such depressions formed in 2016, though depressions that remain above flotation were present in the March through July 2016 profiles. Similar features did not appear in the 2017 and 2018 data, which appear similar to the 2010 and 2011

215   summers when the surface also was well above flotation. When they are present, these depressions advect downstream with the ice flow, as is the case for similar features that have been observed elsewhere (James et al., 2014; Joughin et al., 2008c).

To provide a better picture of the spatial pattern of terminus variation, Fig. 4 shows a subset of the DEMs. In addition to the colour scale to represent elevation, the 100- (white) and 150-m (black) contours are also shown. Below ~100 m, most of the

220 ice in the main trunk should be fully afloat, and above 150 m it should be fully grounded. The region between these contours represents the transition from grounded to floating ice, including the grounding line. As with the profile data, the map-view data reveal periods when the terminus is an abrupt grounded cliff, often indicated by areas where the 100-m contour tracks the terminus. At other times, a heavily crevassed but generally intact floating extension is clearly visible. In particular, the extended tongues that formed during the 2016–17 and 2017–18 winters are still visible in the respective early spring DEMs.

225

The DEMs in Fig. 4 indicate complex spatial and temporal variations in the near terminus geometry. There is a persistent depression that forms in the lee of what appears to be a bed constriction on the north side of the main channel just upstream of the closed white contour in the August 2010 DEM (see Fig. 4). Relatively little thinning occurs on the steep slope immediately upstream of this feature, leading to little variation in the position of 100 and 150-m contours. Towards the centre of the main

230 trunk, however, these contours migrate back and forth ~2.5 km over the observation period, which is consistent with the point data shown in Fig. 2. This variation can yield large changes in the near terminus slope. For example, in July 2012 DEM, the two contours are separated by less than 500 m. By contrast, in the April 2014 DEM the 150 m contour intersects the profile at nearly the same point (diamond in Fig. 4), but the 100-m contour is located nearly 2-km farther downstream. On the south side of the fjord, there is a ridge (e.g., December 2011) that separates a pair of local topographic lows. Over the course of the record,

235 this area evolves substantially as the surface elevation varies by several 10s of meters. There are times when the upstream depression extends inland so that the south side of the channel appears to reach, or at least approach, flotation while the centre and north side remain well grounded. Toward the centre of the main trunk, the ephemeral surface depressions mentioned above are visible in the September 2013 and August 2014 DEMs (see closed contours between the diamond and star in Fig. 4). For many other times, instead of a depression, this region represents a cross-flow high for the main trunk.

240 **4 Discussion**

The results described above provide a detailed view of the evolution of the terminus region of Jakobshavn Isbrae over the last decade. Here we provide additional interpretation, including discussion of the relation between speed and bed topography; how ocean temperature may influence the seasonal speedup through its control on mélange rigidity; the processes that produce surface depressions and related calving events; and ice cliff stability.

245 **4.1 Relation Between Speed and Terminus Position**

As with previous work on Jakobshavn Isbrae (Joughin et al., 2012b), Fig. 2 reveals a strong correlation between seasonal speedup and terminus position. To investigate further, Fig. 5 shows year-by-year linear regressions of terminus speed (T_{max}-1

km) against terminus position. Here we have limited the regressions to positions along the profile >7500 m, which excludes
many of the locations where the terminus was clearly floating and providing little resistance. For all but 2009 and 2010, a
250 linear relation between the two explains >75% of the variance (r^2=0.76–0.92). The lowest correlation occurs in 2010 (r^2=0.32),
which was a year when there was relatively little retreat and corresponding speedup, hence other factors may dominate.

If we consider the terminus position as a proxy for the grounded terminus depth during retreat/advance along a retrograde
slope, then the results in Fig. 5 are consistent with increasing terminus thickness producing speedups during periods of retreat,
255 and vice versa during advance. While this relation should be non-linear (Howat et al., 2005; Thomas, 2004), it appears to be
relatively linear over the scale of the annual perturbations (~2 km) as indicated by the r^2 values. Despite the good agreement,
it is important to note that there is still significant variation not accounted for by terminus position. In particular, some of the
calving events likely occur from a floating or lightly grounded terminus, which should yield little or no speedup (Cassotto et
al., 2019). For example, the brief period of retreat and rapid re-advance in the autumn of 2014 with no corresponding speedup
260 was likely due to calving from a floating ice tongue. In addition, variation in the width of the channel and local bed topography
should also influence speed as the terminus retreats inland.

Both the slope and intercept of the regressions vary substantially over time. The variation in slope to some extent may reflect
the expected non-linearity noted above, with increasing sensitivity as the terminus retreats into deeper water. Faster speeds at
265 less retreated positions in the earlier period (2009–2011) may be due to the generally thicker terminus region (see M6 and M9
elevations in Fig. 2), which should yield a greater surface slope and driving stress in the region upstream of the terminus.

4.2 Role of Ocean Temperature and Mélange

Figure 6 shows ocean temperature (similar to that from Khazendar et al., 2019) and winter air temperature anomalies for the
period from 1980 to the most recent observations. The strong summer speedups from 2012–2015 (Fig. 2) coincide with periods
270 when the water in Disko Bay was relatively warm (>3ºC). Conversely, the slowdown that began in Fall 2016 took place when
the water in Disko Bay was relatively cool (~1.5ºC). Based on this relation, it has been argued that enhanced melting of the
terminus produced greater calving, retreat, and speedup, particularly in summer when buoyant subglacial meltwater plumes
should enhance circulation at the terminus (Khazendar et al., 2019). While water temperature in the fjord should undoubtedly
modulate melt, it is less clear that this correlation establishes a causal relation between enhanced melt at the terminus and
275 speedup/thinning.

Maximum melt rates for 2012 to 2015 are estimated to be ~8-10 m/yr for concentrated plumes with limited spatial extent, or
about a factor 3 less if the melt water emerges with a uniform distribution from beneath the grounded ice (Khazendar et al.,
2019). Whether concentrated or evenly distributed, the factor-of-3 reduction should roughly represent the average melt rate
280 across the terminus. Thus, scaling the plume rates from Khazendar et al. (2019) by a factor of 3 yields approximate average

melt between ~3.5 m/yr during the summers with warmest water and ~1.9 m/yr during the summers when the water was coolest. It is also important to note that much of the oceanic heat in the fjord goes into melting icebergs (Moon et al., 2018), so these values may be biased high. During the summer, the terminus advances at ~30-45 m/day, so that ice is replenished far faster than it is removed via submarine melting at these rates (Joughin et al., 2012a). While we cannot entirely rule out melt
285   serving in some way as a "catalyst" (e.g., by undercutting the front) to accelerate calving, a shift in average melt rate from 3.5 to 1.9 m/yr over a few months of the year should not drastically alter the rate of retreat and speedup.

In contemplating whether submarine melt, particularly in summer, might drive the observed retreat and speedup, it is important to consider the relative timing of the recent changes. Although submarine melt should have been substantially reduced in the
290   summer of 2016 (Khazendar et al., 2019), the maximum retreat was virtually identical to that of the four prior years and speeds were only slightly reduced, suggesting melt is not directly controlling retreat. Unlike prior years in that decade, however, rigid mélange formed early that fall and was uninterrupted for more than 6 months. Over the 2016–17 winter the terminus advanced ~6 km farther than any winter since 2008–09 (Fig. 2), and an even greater re-advance occurred the following winter, which had similar mélange conditions. The additional buttressing from this partially grounded and partially floating extension likely
295   produced much slower summer and winter speeds, which in turn produced the observed thickening (Fig. 3; see also Khazendar et al. 2019). The winter of 2018-2019 yielded a more extended than normal period of rigid mélange, but less so than the previous two winters. In this case, the winter advance fell between the extremes of 2011–2016 and 2016–2018 periods. Collectively, these observations are consistent with earlier work indicating that the presence of rigid mélange can suppress calving (Amundson et al., 2010; Joughin et al., 2008b).

300

Time series of Sentinel 1A/B SAR imagery from 2015-2016 reveal regular flushing of the mélange within the fjord (see movie in Supplement) throughout the summer, consistent with the lack of rigid mélange at the terminus (Fig. 2). By contrast, for most of the winter the mélange moves down much of the fjord at the rate at which it is pushed by the terminus. While not as regular as in the summer, there were several flushing events in the winter of 2015–16, during which a large portion of the mélange
305   was rapidly advected through and cleared from the fjord. In the 2016–17 and 2017-18 cold seasons, however, the first flushing events did not occur until April and May, respectively, consistent with an indication of more rigid mélange shown in Fig. 2.

It is well established that rigid mélange is most prevalent in winter when surface air temperatures are low (Cassotto et al., 2015), which agrees with the results in Fig. 2. Nearby weather station data (Fig. 6) indicate that the 2016–17 and 2017–18
310   winters were colder than normal for the decade, but so was the 2014–15 winter that was followed by a large summer speedup, suggesting that air temperatures are not the only control. As noted above, 250-m water temperatures in Disko Bay were ~1.5ºC cooler for 2016-2017 (Fig. 6 and Khazendar et al., 2019), and this cold ocean layer should extend across the sill at the mouth of the fjord (Gladish et al., 2015a). A reasonable assumption is that this colder water facilitated more rapid winter freeze up and greater mélange rigidity in the winter of 2016–17, with similar behavior the subsequent winters. By contrast, the warmer

315 layer of water present from 2011–2015 likely facilitated greater mélange mobility, which allowed greater calving throughout the corresponding winters. This hypothesis is consistent with the finding that much of the oceanic heat in the fjord contributes to iceberg melting (Moon et al., 2018).

The 2010–11 winter is interesting because the amplitude of the annual cycle of terminus advance and retreat was reduced
320 relative to other winters (Fig. 2). Periods of rigid mélange were sporadic, but occurred relatively early in the autumn and relatively late in the spring. Ocean temperatures were also exceptionally cool in 2010 (Fig. 6 and Gladish et al., 2015b), which may have contributed to the formation of the more rigid mélange that was present at times during the late spring and early fall. By contrast, the 2010 and 2011 winter air temperatures preceding and following summer 2010 were the warmest since before 1980 (Fig. 6), which may have reduced the formation of rigid mélange in winter. Thus, both oceanic and atmospheric forcing,
325 acting counter to the "normal" seasonal cycle, may have played a role in the unusual retreat pattern for 2010. Thus, while the influence of ocean temperature may be the dominant factor in the formation of rigid mélange, air temperature may play a secondary role in determining interannual variability of mélange rigidity. Furthermore, although we do not have good data on the seasonal variation in ocean temperature, certainly there is a strong correspondence between seasonal variation in air temperature and mélange rigidity. Thus our observations suggest that while recent fluctuations in ocean temperature over the
330 last decade may have governed much of the flow variability on Jakobshavn Isbrae (Khazendar et al., 2019), the prime link between ice flow and water temperature is its effect on mélange rigidity, not submarine melting at the terminus.

The data in Fig. 6 show both cooler ocean and atmospheric temperatures prior to the late 1990s speedup, consistent with higher sea-ice concentration in Disko Bay during this period (Joughin et al., 2008b). The original breakup of the floating ice tongue
335 in the late 1990s early 2000s and the subsequent speedup has been attributed to both reduced mélange rigidity (Joughin et al., 2008b) and greater submarine melting (Holland et al., 2008; Motyka et al., 2011). Unlike the case in recent years when the terminus often had a vertical face with limited area in contact with the ocean, the area of the former 15-km long, several hundred-meter-thick floating tongue that was exposed to high melt rates was more than an order of magnitude greater. In this case, a basal melt rate increase of 1 m/day or more could have had a strong effect on the ice tongue viability, as earlier work
340 has noted (Holland et al., 2008; Motyka et al., 2011). From 1962 to 1996, there was a strong seasonal variation in calving likely driven by mélange rigidity (Sohn et al., 1998), which could have been amplified as ocean and air temperatures increased. While submarine melting may have thinned the ice shelf substantially, thin ice can remain intact for long periods when embedded in perennial sea ice or strong mélange (Reeh et al., 2001). Since both processes would have been acting at the same time, it may have been their combined effects that eliminated the ice tongue and triggered the speedup. In addition, enhanced
345 hydrofracturing due to increased surface meltwater may have played a role in breaking up the ice tongue (Scambos et al., 2000; Sohn et al., 1998).

4.3 Depressions Leading to Calving Events

Beginning in 2012 and extending through at least 2015, a series of transverse depressions developed behind the terminus prior to several late summer and autumn calving events (Fig. 3). The bottoms of some of these depressions extend more than 50 m
350   below flotation, and appear to eventually serve as the detachment points for large calving events. Downstream of these depressions, the area immediately upstream of the terminus can reach heights of 25 m or more above flotation. Similar features have been observed on Helheim and Kangerdlugssuaq glaciers (Howat et al., 2007; James et al., 2014; Joughin et al., 2008c), and the development of one on Jakobshavn Isbrae was captured with a terrestrial radar interferometer in August 2012 (Cassotto et al., 2019). These features, which develop over weeks, are distinctly different than the depressions that can form as the
355   terminus rises above flotation for tens of minutes prior to large calving events (Parizek et al., 2019).

To better examine the evolution of one of these depressions in 2015, Figs. 7 and 8 show a time series of elevations in profile- and map-view, respectively. To improve temporal sampling, Fig. 8 also shows several TerraSAR-X images. The imaging geometry for these acquisitions was such that a prominent radar shadow is visible when there is a steep, high terminus, (e.g.,
360   August 24). In addition, sufficiently well-developed depressions are distinguishable in the SAR data (e.g. September 26). The general pattern of brightening with time in the SAR image time series is due to the transition from summer melting to fall freeze-up. To track the evolution of the parcel of ice that evolves to form the bottom of a large depression, we used the average velocity field for this period to estimate its location through time, which is shown with coloured triangles in Fig. 7 and white dots in Fig. 8.
365

In the July 31 and August 5 DEMs, a minor depression near flotation was apparent (Fig. 7), which is difficult to identify in the SAR images from this period (Fig. 8). These first two DEMs and the SAR data reveal a nearly vertical calving face ~120–140 m high. By August 13, the less pronounced shadow in the SAR image indicates a less sheer terminus and the development of several large crevasses or, potentially, through-going rifts. By August 22 a large calving event, which appears to have extended
370   through the bottom of the minor depression, produced a steep new calving face ~130 m high. Although the August 22 DEM is limited in extent, there is a shallow back slope at the upstream end that suggests the presence of a nascent depression, which is not yet distinguishable in the radar image from 2 days later. By September 4, however, there is a subtle indication of this depression in the radar data (see area around white circle for September 4 in Fig. 8). The September 14 elevation data show that the bottom of the depression was ~40-m below flotation (Figs. 7&8). Over the next 16 days, this feature advected
375   downstream, deepening to ~65 meters below flotation. Although the spatial scale is such that the area below flotation is not fully in hydrostatic equilibrium, its depth suggests thinning by up to several hundred meters.

Depressions below flotation that develop through-going rifts and form detachment points for icebergs represent one mode of calving (James et al., 2014; Joughin et al., 2008c). One mechanism that has been proposed to explain this evolution involves

380 a grounded glacier advancing down a prograde (forward) slope, driving the terminus downward, causing buoyant flexure that lifts the front above flotation but depresses the region upstream below flotation (James et al., 2014; Wagner et al., 2016). This process does not seem to apply here because both the available bed topography and the observed speed as function of terminus position (e.g., Fig. 5) are consistent with a retrograde rather than prograde bed slope. Moreover, the glacier surface is above flotation both upstream and downstream of the depression, which means if it was purely the result of downward flexure of ice

385 initially above flotation then its base would have to dip below the bed. Alternatively, flow models illustrate that reverse surface slopes can develop near the terminus of an outlet glacier, but these features are generally tied to the underlying topography and do not advect downstream as do the depressions shown in Figs. 7 and 8 (Vieli et al., 2002).

In general, the depressions we observe tend to develop after summer thinning yields a surface near flotation in the region a

390 few kilometres upstream of the terminus. Strong extension near the terminus and an ice column that is at or near flotation should facilitate the development of basal crevasses (Van Der Veen, 1998). Once a basal crevasse develops, the thinner ice above it must support the same column-integrated longitudinal stress, leading to greater extension. As a result, a necking process likely would commence, causing sustained localized thinning that would create depressions like those shown in Figs. 3, 7, and 8 (Bassis and Ma, 2015). Consistent with this hypothesis, the observed depressions have width/thickness ratios (~1:1)

395 similar to modelled results (Bassis and Ma, 2015). Furthermore, Fig. 7 shows the velocity gradient steepening over the areas where the depressions occur, which is consistent with that increased strain rates and thinning that forms them.

As the depressions develop, the elevation downstream of the depression and ~1 km upstream of the terminus remains tens of meters above flotation (Figs. 7 and 8). While similar high spots have been attributed to buoyant flexure on Helheim (James et

400 al., 2014), in the examples presented here, the downstream high spot seems to be advected downstream faster than it can thin to flotation (see progression of high spot from August 22 to September 30). After it attains a peak value, strong extension produces thinning so that the last few hundred meters of the heavily rifted terminus regions are afloat.

The development of depressions like those just described occurred over several weeks, culminating in large calving events

405 involving a kilometre or more of ice (e.g., August 22 to October 11 in Figs. 7 and 8). Such events seem to occur in late summer to early fall and did not start until 2012. As Fig. 3 indicates, in 2010 and 2011 the near-terminus region was relatively steep, rising quickly above flotation, making it less likely that basal crevasses will form upstream of the terminus at these times. The more intense summer speedups that began in 2012, however, produced shallower late-summer calving fronts, with elevations near flotation extending several kilometres upstream of the terminus, which were favourable to basal crevasse formation that could seed the formation of these depressions. Thus, this mode of calving appears generally to occur in late summer after

410 strong speedups have produced conditions favourable to the formation of basal crevasses that can evolve to form surface depressions. Since full-thickness calving requires a terminus near flotation (Amundson et al., 2010), the development of the high spot downstream of the depression may suppress calving long enough to give these features more time to develop.

4.4 Terminus Elevation and Cliff Instability

415   The depressions that lead to the calving events described above represent just one of a variety of failure modes that can cause calving. Recent work has raised concern about ice cliff instability contributing to rapid ice-sheet collapse (DeConto and Pollard, 2016). With ice cliffs more than 130 m above the waterline at times, Jakobshavn Isbrae provides an interesting case study for understanding the effect of such potential instabilities. In actuality, however, ice sheet or glacier instability arises when the calving and discharge rates fall out of sync (Amundson and Truffer, 2010), rather from the actual failures (i.e.,

420   calving events). Whether it initiates above or below the water line, it is important to note that some kind of material failure must occur to produce calving events even in steady state. It is also important to consider that while the terminus is advancing at 40 m/day and calving in ~100 m slabs, any ice cliff has a limited lifespan (~2.5 days on average, though clustering of calving events may keep some cliffs intact up to weeks). Here we examine evolution of the front, following the formation of steep calving faces.

425

Figure 7 illustrates the evolution of what begins as an initially ~130-m high sheer ice front (see August 22 in Fig. 7). Rather than a brittle failure event leading to a rapid collapse, the strong extension near the terminus instead causes evolution from a sheer grounded cliff to a heavily crevassed floating tongue with a ~5% slope (see September 30 in Fig. 7). In some sense this represents the failure of the cliff, but as a process that evolves over weeks likely involving multiple small failures (e.g., crevasse

430   events) rather than a single catastrophic failure. Furthermore, the stability of the floating extension depends on environmental factors. As our data suggest, cooler ocean temperatures, perhaps supplemented by colder air temperatures, could allow such a tongue to advance over the colder part of the year. Conversely, when more summer-like conditions prevail, such a tongue should disintegrate far more rapidly as was the case for the transient tongue shown in shown in Figs. 7 and 8. Thus, stability likely is governed more by environmental conditions than by a single height-dependent mechanical failure criterion that could

435   yield rapid collapse (Parizek et al., 2019).

Our data also reveal that once the summer speedup commences, near terminus surface thinning rates can exceed 50 m over the course of a few months (see M6 elevations in Fig. 2). Thus, even without cliff failure, the high stretching rates associated with an unbuttressed terminus on a retrograde bed slope can cause rapid thinning to flotation, which, if unabated, will lead to further

440   calving and rapid retreat. Were it not for the seasonal cycle that facilitates re-advance and winter thickening (see Figs. 2 and 3), the terminus of Jakobshavn Isbrae would have receded far deeper inland than it has thus far, even without ice cliff collapse as such.

Finally, it is important to note that to the best of our knowledge, Jakobshavn Isbrae has the deepest unbuttressed calving face

445   in Greenland or Antarctica, leading to the fastest marine terminating glaciers speeds (Joughin et al., 2014). As such, it has been out of balance at times by more than a factor of 3 seasonally (Joughin et al., 2014) and a factor of 2 annually (Mouginot et al.,

2019). Nearly all glaciers in Greenland and Antarctica have steady-state speeds well below that of Jakobshavn Isbrae. Thus, given that speed scales non-linearly with terminus depth (Schoof, 2007), any glacier that evolves to the point where the height of its unbuttressed calving face rivals that of Jakobshavn Isbrae will already be well out of balance, yet likely will maintain 450 heights well below those needed to exceed a material failure criterion (~200 m) that would lead to rapid brittle failure (Parizek et al., 2019). Our point is not that cliff failure is irrelevant, but rather that any glacier that reaches terminus heights where cliff failure may be a significant effect, must already be in a state of rapid retreat. Far more important to long-term outlet glacier stability is how seasonal variability and oceanographic/atmospheric trends influence the calving rates of grounded glacier termini. In Antarctica and northern Greenland there are additional atmospheric temperature sensitivities (e.g., meltwater 455 ponding and hydrofracture) that influence ice-shelf stability (Scambos et al., 2000). In summary, while brittle failure cliff instability may be important in some circumstances, it is far more likely to play a role in a late stage retreat than to serve as the process that would initiate such a retreat.

5 Conclusions

We have assembled and produced a comprehensive time series of surface flow velocity, surface elevation, and mélange rigidity 460 for Jakobshavn Isbrae over the last decade. The data show a strong degree of variability, including a potentially brief slowdown that coincided with cooler ocean temperatures (see also Khazendar et al., 2019). The time series of elevation provides an unprecedented level of detail, which clearly shows a pattern of summer thinning partially offset by winter thickening in response to seasonal changes in flow speed. These data also provide observational evidence to support theoretical development describing how necking proceeds as basal crevasses form (Bassis and Ma, 2015). They also show that although Jakobshavn 465 Isbrae likely has the highest unbuttressed ice cliffs on Earth, at this point they do not appear to be subject to catastrophic brittle failure. Most importantly, our observations reinforce earlier findings on the influence of mélange rigidity on calving (Amundson et al., 2010; Joughin et al., 2008b), and help establish a connection to ocean temperature. Water temperatures are expected to rise over the next century (Stocker et al., 2013), which will likely produce further retreat of Jakobshavn Isbrae. Superimposed on any trend for the last century, however, there is substantial multi-decadal scale variability of ocean 470 temperatures in Disko Bay that correlate well with the Atlantic Multidecadal Oscillation (AMO) Index, which has been linked to past changes on Jakobshavn Isbrae (Lloyd et al., 2011). Thus, whether Jakobshavn Isbrae can stabilize, at least temporarily, likely depends on whether a cycle similar to that of the last century produces an extended period of cooler waters in Disko Bay.

Acknowledgements

475 The National Aeronautics and Space Administration (NASA) supported contributions by I.J. (NNX17AH04G), D.S. (NESSF fellowship award NNX12AN36H), and B.S. (NNX13AP96G). Resources supporting this work were provided by the NASA

High-End Computing (HEC) Program through the NASA Advanced Supercomputing (NAS) Division at Ames Research Center. The TerraSAR-X and TanDEM-X data were provided by DLR (project HYD0754 and XTI_GLAC0400). The Cosmo-SkyMed data were delivered under an ASI licence to use. The bed data were provided by the BedMachine project at UC Irvine

480 and archived at NSIDC (https://nsidc.org/data/IDBMG4). Ocean temperature date were provided by the Ocean Melting Greenland Project (OMG) and the International Council for the Exploration of the Sea Oceanography. Weather station data were provided by the Goddard Institute for Space Studies GISTEMP Team. We acknowledge Claire Porter, Paul Morin, and others at the Polar Geospatial Center (NSF ANT-1043681) who managed tasking, ordering, and distribution of the L1B commercial stereo imagery under the NGA NextView license. DEMs provided by the Polar Geospatial Center under NSF-

485 OPP awards 1043681, 1559691, and 1542736. Comments by M. Maki improved the manuscript.

References

Amundson, J. M. and Truffer, M.: A unifying framework for iceberg-calving models, J Glaciol, 56(199), 822–830, 2010.

Amundson, J. M., Fahnestock, M., Truffer, M., Brown, J., Luethi, M. P. and Motyka, R. J.: Ice melange dynamics and

490 implications for terminus stability, Jakobshavn Isbrae Greenland, J Geophys Res-Earth, 115, F01005, doi:10.1029/2009JF001405, 2010.

Bassis, J. N. and Ma, Y.: Evolution of basal crevasses links ice shelf stability to ocean forcing, Earth Planet Sc Lett, 409, 203–211, doi:10.1016/j.epsl.2014.11.003, 2015.

Beyer, R. A., Alexandrov, O. and McMichael, S.: The Ames Stereo Pipeline: NASA's Open Source Software for Deriving

495 and Processing Terrain Data, Earth and Space Science, 5(9), 537–548, doi:10.1029/2018EA000409, 2018.

Cassotto, R., Fahnestock, M., Amundson, J. M., Truffer, M. and Joughin, I.: Seasonal and interannual variations in ice melange and its impact on terminus stability, Jakobshavn Isbrae, Greenland, J Glaciol, 61(225), 76–88, doi:10.3189/2015JoG13J235, 2015.

Cassotto, R., Fahnestock, M., Amundson, J. M., Truffer, M., Boettcher, M. S., la Pena, de, S. and Howat, I.: Non-linear

500 glacier response to calving events, Jakobshavn Isbrae, Greenland, J Glaciol, 65(249), 39–54, doi:10.1017/jog.2018.90, 2019.

Cuffey, K. M. and Paterson, W.: The Physics of Glaciers, 4 ed., Amsterdam. 2010.

DeConto, R. M. and Pollard, D.: Contribution of Antarctica to past and future sea-level rise, Nature, 531(7596), 591–597, doi:10.1038/nature17145, 2016.

Echelmeyer, K. and Harrison, W. D.: Jakobshavns Isbræ, West Greenland: Seasonal variations in velocity-or lack thereof, J

505 Glaciol, 36(122), 82–88, 1990.

GISTEMP Team 2019: *GISS Surface Temperature Analysis (GISTEMP), version 4*, [online] Available from: https://data.giss.gov/gistemp, 2019.

Gladish, C. V., Holland, D. M. and Lee, C. M.: Oceanic Boundary Conditions for Jakobshavn Glacier. Part II: Provenance and Sources of Variability of Disko Bay and Ilulissat Icefjord Waters, 1990-2011, J Phys Oceanogr, 45(1), 33–63, doi:10.1175/JPO-D-14-0045.1, 2015a.

510

Gladish, C. V., Holland, D. M., Rosing-Asvid, A., Behrens, J. W. and Boje, J.: Oceanic Boundary Conditions for Jakobshavn Glacier. Part I: Variability and Renewal of Ilulissat Icefjord Waters, 2001-14, J Phys Oceanogr, 45(1), 3–32, doi:10.1175/JPO-D-14-0044.1, 2015b.

Hoehle, J. and Hoehle, M.: Accuracy assessment of digital elevation models by means of robust statistical methods, ISPRS Journal of Photogrammetry and Remote Sensing, 64(4), 398–406, doi:10.1016/j.isprsjprs.2009.02.003, 2009.

515

Holland, D. M., Thomas, R. H., De Young, B., Ribergaard, M. H. and Lyberth, B.: Acceleration of Jakobshavn Isbrae triggered by warm subsurface ocean waters, Nat Geosci, 1(10), 659–664, doi:10.1038/ngeo316, 2008.

Howat, I. M., Joughin, I. and Scambos, T.: Rapid Changes in Ice Discharge from Greenland Outlet Glaciers, Science, 315(5818), 1559–1561, doi:10.1126/science.1138478, 2007.

520 Howat, I. M., Joughin, I., Tulaczyk, S. and Gogineni, S.: Rapid retreat and acceleration of Helheim Glacier, east Greenland, Geophys Res Lett, 32(22), L22502, doi:10.1029/2005GL024737, 2005.

James, T. D., Murray, T., Selmes, N., Scharrer, K. and O'Leary, M.: Buoyant flexure and basal crevassing in dynamic mass loss at Helheim Glacier, Nat Geosci, 7(8), 594–597, doi:10.1038/NGEO2204, 2014.

Joughin, I.: Ice-sheet velocity mapping: A combined interferometric and speckle-tracking approach, Ann Glaciol, 34, 195–
525 201, 2002.

Joughin, I. R., Kwok, R. and Fahnestock, M. A.: Interferometric estimation of three-dimensional ice-flow using ascending and descending passes, IEEE T Geosci Remote, 36(1), 25–37, 1998.

Joughin, I., Abdalati, W. and Fahnestock, M.: Large fluctuations in speed on Greenland's Jakobshavn Isbræ glacier, Nature, 432(7017), 608–610, doi:10.1038/nature03130, 2004.

530 Joughin, I., Alley, R. B. and Holland, D. M.: Ice-sheet response to oceanic forcing, Science, 338(6111), 1172–1176, doi:10.1126/science.1226481, 2012a.

Joughin, I., Das, S. B., King, M. A., Smith, B. E., Howat, I. M. and Moon, T.: Seasonal speedup along the western flank of the Greenland Ice Sheet, Science, 320(5877), 781–783, doi:10.1126/science.1153288, 2008a.

Joughin, I., Howat, I. M., Fahnestock, M., Smith, B., Krabill, W., Alley, R. B., Stern, H. and Truffer, M.: Continued
535 evolution of Jakobshavn Isbrae following its rapid speedup, J Geophys Res-Earth, 113, F04006, doi:10.1029/2008JF001023, 2008b.

Joughin, I., Howat, I., Alley, R. B., Ekstrom, G., Fahnestock, M., Moon, T., Nettles, M., Truffer, M. and Tsai, V. C.: Ice-front variation and tidewater behavior on Helheim and Kangerdlugssuaq Glaciers, Greenland, J Geophys Res-Earth, 113, –, doi:10.1029/2007JF000837, 2008c.

540 Joughin, I., Smith, B. E. and Howat, I.: Greenland Ice Mapping Project: ice flow velocity variation at sub-monthly to decadal timescales, The Cryosphere, 12(7), 2211–2227, doi:10.5194/tc-12-2211-2018, 2018.

Joughin, I., Smith, B. E., Howat, I. M., Floricioiu, D., Alley, R. B., Truffer, M. and Fahnestock, M.: Seasonal to decadal scale variations in the surface velocity of Jakobshavn Isbrae, Greenland: Observation and model-based analysis, J Geophys Res, 117(F2), F02030, doi:10.1029/2011JF002110, 2012b.

545   Joughin, I., Smith, B. E., Shean, D. E. and Floricioiu, D.: Brief Communication: Further summer speedup of Jakobshavn Isbrae, The Cryosphere, 8(1), 209–214, doi:10.5194/tc-8-209-2014, 2014.

Khazendar, A., Fenty, I. G., Carroll, D., Gardner, A., Lee, C. M., Fukumori, I., Wang, O., Zhang, H., Seroussi, H., Moller, D., Noel, B. P. Y., Van Den Broeke, M. R., Dinardo, S. and Willis, J.: Interruption of two decades of Jakobshavn Isbrae acceleration and thinning as regional ocean cools, Nat Geosci, 12(4), 277–+, doi:10.1038/s41561-019-0329-3, 2019.

550   Krabill, W., Hanna, E., Huybrechts, P., Abdalati, W., Cappelen, J., Csatho, B., Frederick, E., Manizade, S., Martin, C., Sonntag, J., Swift, R., Thomas, R. and Yungel, J.: Greenland Ice Sheet: Increased coastal thinning, Geophys Res Lett, 31(24), L24402, doi:10.1029/2004GL021533, 2004.

Lemos, A., Shepherd, A., McMillan, M., Hogg, A. E., Hatton, E. and Joughin, I.: Ice velocity of Jakobshavn Isbræ, Petermann Glacier, Nioghalvfjerdsfjorden, and Zachariæ Isstrøm, 2015–2017, from Sentinel 1-a/b SAR imagery, The
555   Cryosphere, 12(6), 2087–2097, doi:10.5194/tc-12-2087-2018, 2018.

Lloyd, J., Moros, M., Perner, K., Telford, R. J., Kuijpers, A., Jansen, E. and McCarthy, D.: A 100 yr record of ocean temperature control on the stability of Jakobshavn Isbrae, West Greenland, Geology, 39(9), 867–870, doi:10.1130/G32076.1, 2011.

Luckman, A. and Murray, T.: Seasonal variation in velocity before retreat of Jakobshavn Isbrae, Greenland, Geophys Res
560   Lett, 32(8), L08501, doi:10.1029/2005GL022519, 2005.

Moon, T., Sutherland, D. A., Carroll, D., Felikson, D., Kehrl, L. and Straneo, F.: Subsurface iceberg melt key to Greenland fjord freshwater budget, Nat Geosci, 11(1), 49–54, doi:10.1038/s41561-017-0018-z, 2018.

Morlighem, M., Williams, C. N., Rignot, E., An, L., Arndt, J. E., Bamber, J. L., Catania, G., Chauche, N., Dowdeswell, J. A., Dorschel, B., Fenty, I., Hogan, K., Howat, I., Hubbard, A., Jakobsson, M., Jordan, T. M., Kjeldsen, K. K., Millan, R.,
565   Mayer, L., Mouginot, J., Noel, B. P. Y., O'Cofaigh, C., Palmer, S., Rysgaard, S., Seroussi, H., Siegert, M. J., Slabon, P., Straneo, F., van den Broeke, M. R., Weinrebe, W., Wood, M. and Zinglersen, K. B.: BedMachine v3: Complete Bed Topography and Ocean Bathymetry Mapping of Greenland From Multibeam Echo Sounding Combined With Mass Conservation, Geophys Res Lett, 44(21), 11051–11061, doi:10.1002/2017GL074954, 2017.

Motyka, R. J., Truffer, M., Fahnestock, M., Mortensen, J., Rysgaard, S. and Howat, I.: Submarine melting of the 1985
570   Jakobshavn Isbrae floating tongue and the triggering of the current retreat,, 116(F1), –n–a, doi:10.1029/2009JF001632, 2011.

Mouginot, J., Rignot, E., Bjork, A. A., van den Broeke, M., Millan, R., Morlighem, M., Noël, B., Scheuchl, B. and Wood, M.: Forty-six years of Greenland Ice Sheet mass balance from 1972 to 2018, P Natl Acad Sci USA, 116(19), 9239–9244, doi:10.1073/pnas.1904242116, 2019.

575   Noh, M.-J. and Howat, I. M.: The Surface Extraction from TIN based Search-space Minimization (SETSM) algorithm, ISPRS Journal of Photogrammetry and Remote Sensing, 129, 55–76, doi:10.1016/j.isprsjprs.2017.04.019, 2017.

Parizek, B. R., Christianson, K., Alley, R. B., Voytenko, D., Vankova, I., Dixon, T. H., Walker, R. T. and Holland, D. M.: Ice-cliff failure via retrogressive slumping, Geology, 47(5), 449–452, doi:10.1130/G45880.1, 2019.

Porter, C., Morin, P., Howat, I., Noh, M.-J., Bates, B., Peterman, K., Keesey, S., Schlenk, M., Gardiner, J., Tomko, K.,
580   Willis, M., Kelleher, C., Cloutier, M., Husby, E., Foga, S., Nakamura, H., Platson, M., Wethington, M. J., Williamson, C.,
Bauer, G., Enos, J., Arnold, G., Kramer, W., Becker, P., Doshi, A., D'Souza, C., Cummens, P., Laurier, F. and Bojesen, M.:
ArcticDEM,, (2018-09-26), 2018–09–26, doi:10.7910/DVN/OHHUKH, 2018.

Reeh, N., Thomsen, H., Higgins, A. and Weidick, A.: Sea ice and the stability of north and northeast Greenland floating
glaciers, Ann Glaciol, 33, 474–480, 2001.

585   Scambos, T., Hulbe, C., Fahnestock, M. and Bohlander, J.: The link between climate warming and break-up of ice shelves in
the Antarctic Peninsula, J Glaciol, 46(154), 516–530, 2000.

Schoof, C.: Ice sheet grounding line dynamics: Steady states, stability, and hysteresis, J Geophys Res-Earth, 112(F3),
F03S28, doi:10.1029/2006JF000664, 2007.

Shean, D. E.: Quantifying ice-shelf basal melt and ice-stream dynamics using high-resolution DEM and GPS time series,
590   PhD Thesis University of Washington, Seattle, 9 June. 2016.

Shean, D. E., Moratto, Z. M., Alexandrov, O., B, S., I, J., C, P. and P, M.: An automated, open-source pipeline for mass
production of digital elevation models from very-high-resolution commerical stereo satellite imagery, SPRS Journal of
Photogrammetry and Remote Sensing, doi:in review, 2015.

Sohn, H. G., Jezek, K. C. and Van der Veen, C. J.: Jakobshavn Glacier, West Greenland: 30 years of spaceborne
595   observations, Geophys Res Lett, 25(14), 2699–2702, 1998.

Stocker, T. F., Qin, D., Plattner, G. K., Tignor, M., Allen, S. K., Boschung, J., Nauels, A., Xia, Y., Bex, V. and Midgley, P.
M.: Climate Change 2013 - The Physical Science Basis, edited by Intergovernmental Panel on Climate Change, T. F.
Stocker, Q. Ding, G. K. Plattner, M. Tignor, S. K. Allen, J. Boschung, A. Nauels, Y. Xia, V. Bex, and P. M. Midgley,
Cambridge University Press, Cambridge. 2013.

600   Thomas, R. H.: Force-perturbation analysis of recent thinning and acceleration of Jakobshavn Isbræ, Greenland, J Glaciol,
50(168), 57–66, 2004.

Thomas, R. H., Abdalati, W., Frederick, E., Krabill, W., Manizade, S. and Steffen, K.: Investigation of surface melting and
dynamic thinning on Jakobshavn Isbrae, Greenland, J Glaciol, 49(165), 231–239, 2003.

Van Der Veen, C.: Fracture mechanics approach to penetration of bottom crevasses on glaciers, Cold Reg Sci Technol,
605   27(3), 213–223, 1998.

Wagner, T. J. W., James, T. D., Murray, T. and Vella, D.: On the role of buoyant flexure in glacier calving, Geophys Res
Lett, 43(1), 232–240, doi:10.1002/2015GL067247, 2016.

610
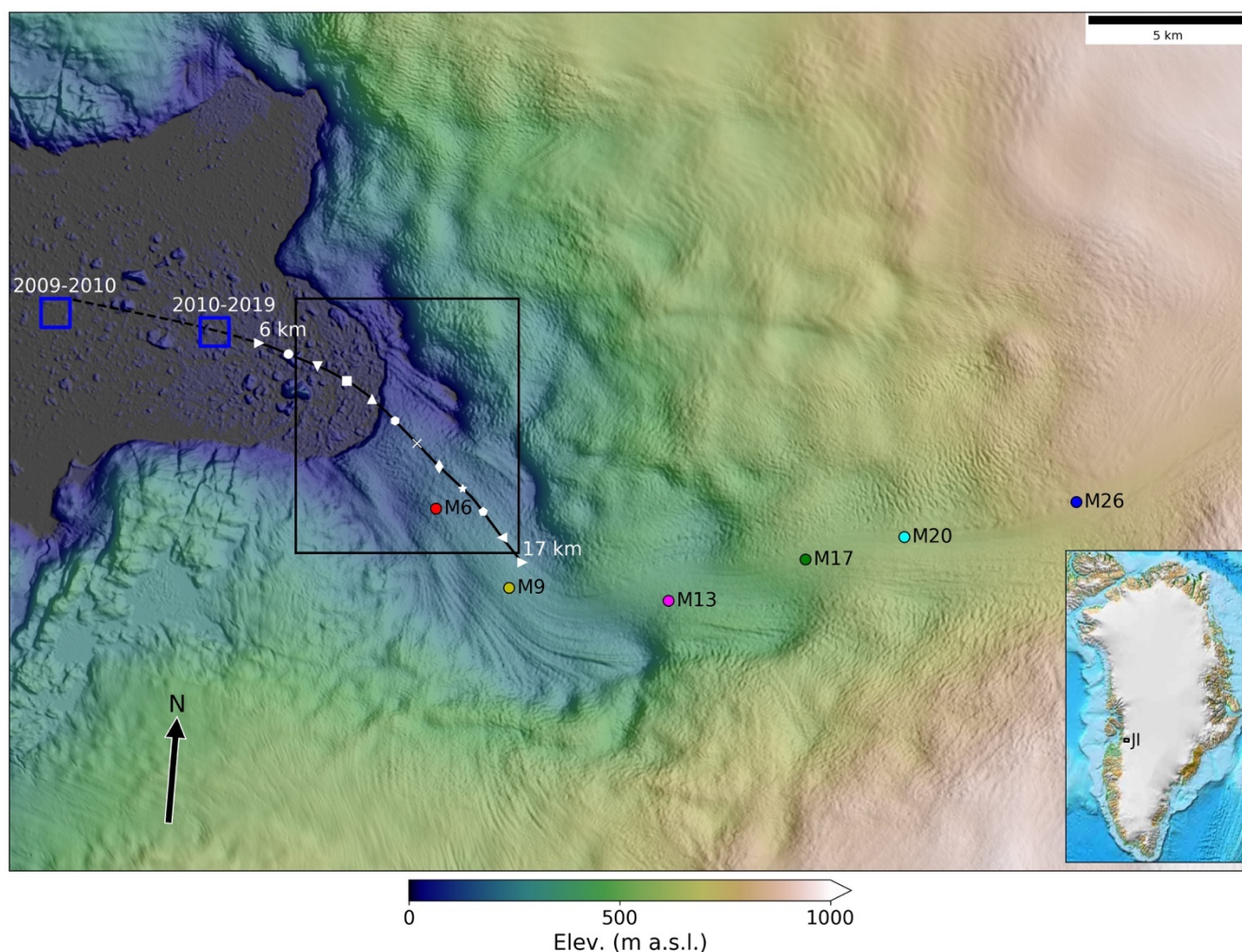
Figure 1: Surface elevation (colour) over shaded surface derived from the GIMP DEM for the region near the terminus of Jakobshavn Isbrae (see inset for location). The black box shows location of images shown in Figs. 4 and 8 and the blue box indicates area used to sample mélange as described in the text. The solid black line shows the location of the profile shown in Figs. 3 and BB, with the dashed section used to show the full extent. White markers with assorted symbols denote 1-km intervals along the profile between 6- and 17-km. Coloured markers (M6-M26) show where velocity is sampled in Fig. 2 at points consistent with earlier work (Joughin et al., 2008b; 2012b; 2014).
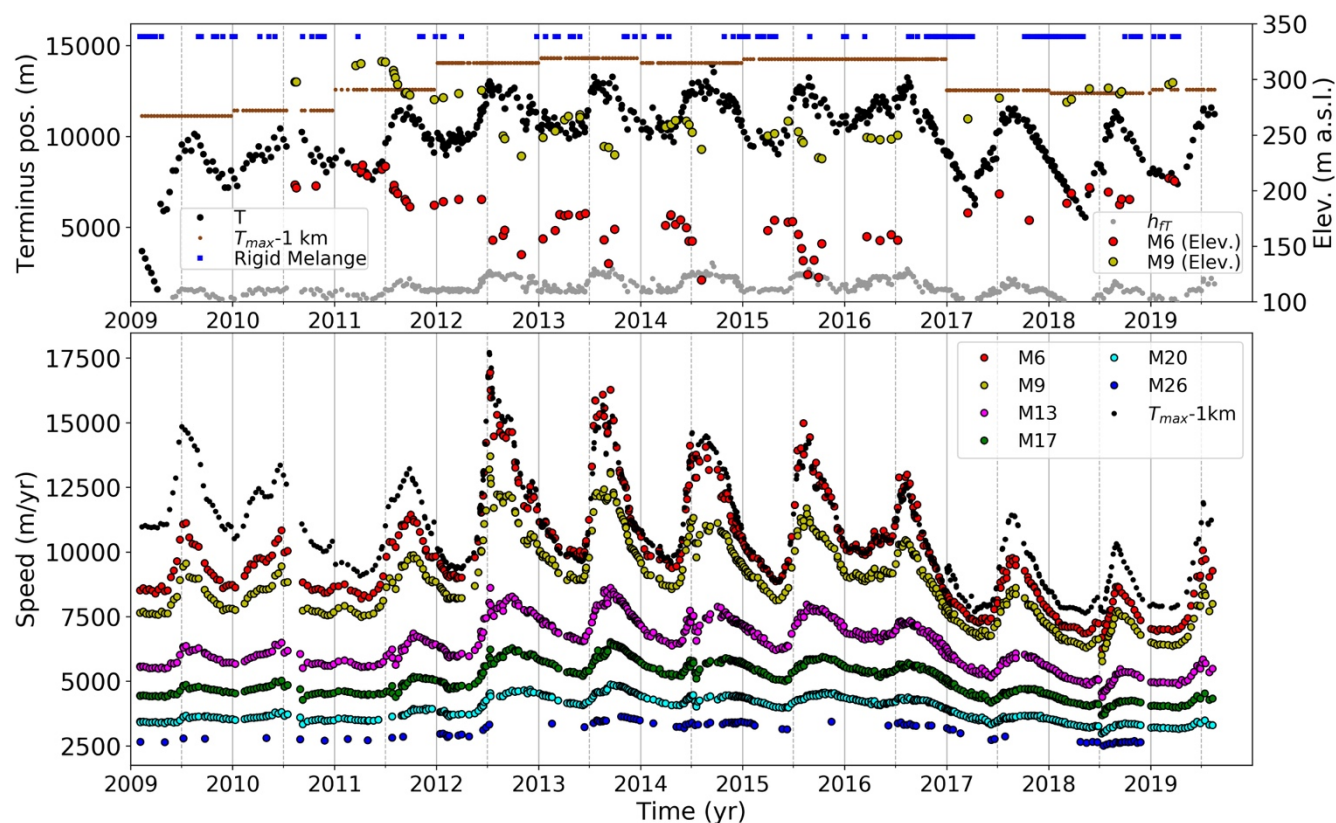
Figure 2. (top) Terminus position (T: black circles), and position 1-km upstream of annual minimum terminus extent ($T_{max} − 1km$: brown) at points along our profile (black line Fig. 1). Two points in 2014 were excluded in determining $T_{max} − 1km$ (see text). The 2019 position will likely recede further as the summer progresses. The blue points indicate when rigid mélange was present in front of the terminus at the location indicated by the blue boxes in Fig. 1. Elevation of the point M6 extracted from all available DEMs is also shown (red) along with the flotation height, h_{fT}, (grey) at the terminus. (bottom) Speeds through time derived from the updated TerraSAR-X/TanDEM-X velocity time series, with a few points from summer 2019 derived using COSMO-SkyMed data. See Fig. 1 for locations of points M6-M26. The black circles indicate the speed at $T_{max} − 1km$. Because this minimum is updated annually, unlike the other points, there are discontinuities at each year boundary since the sampling point location changes (e.g., brown points in the top plot).

635
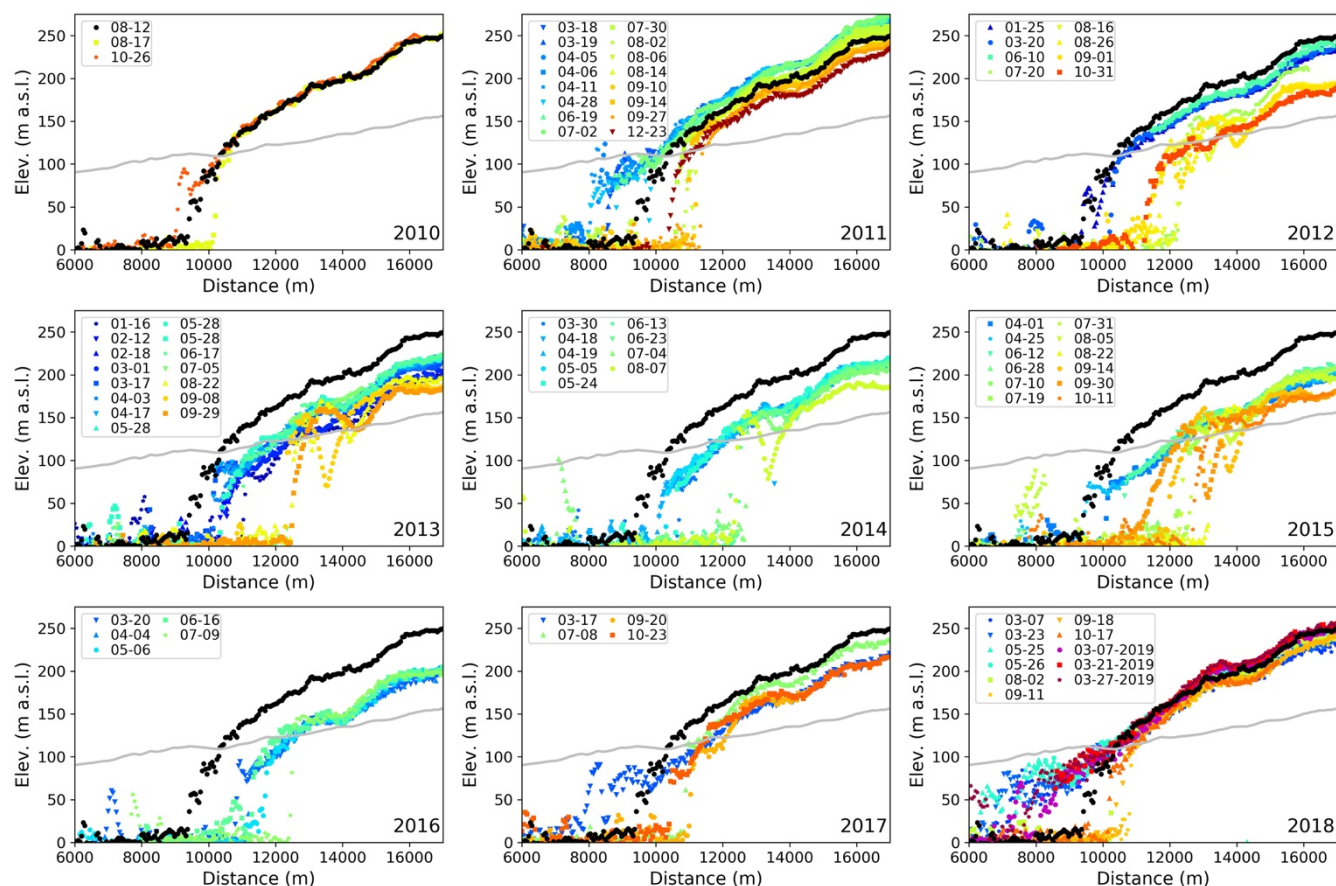
Figure 3. Plots of available near-terminus elevation profiles from 2010 through 2018, with three 2019 profiles included in the 2018 plot. Profiles are labelled by date (MM-DD). Profile location is shown in Fig. 1. For reference, the initial 2010 profile (2010-08-12) is included in each plot. All elevations are relative to nominal mean sea-level (EGS2008 geoid). The grey line indicates the approximate flotation height as determined using bed elevations (Fig. S1) from BedMachine v3 (Morlighem et al., 2017).

640
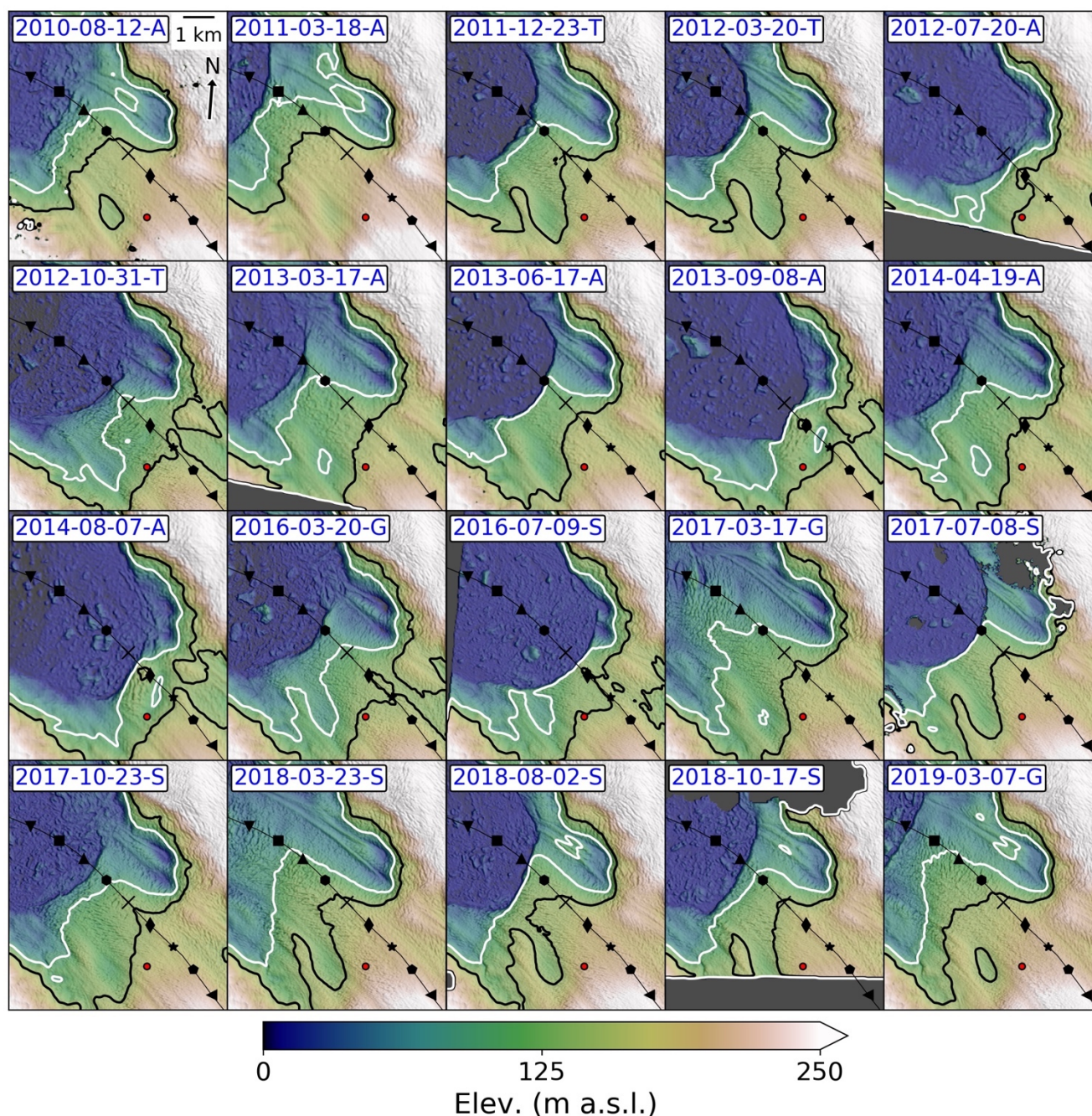
Figure 4. Color shaded relief maps for of a subset of DEMs, excluding maps for 2015, which are included in Fig. 8. Elevation contours of 150 (black) and 100 (white) meters bound the approximate transition from grounded to floating ice. The letter after the date-string (YYYY-MM-DD) indicates the DEMs source (A: ASP World View, T: TanDEM-X, S: SETSM World View, and G: GLISTIN). The profile with 1-km symbols is the same as shown in Fig. 1 and the red dot shows the location of M6.
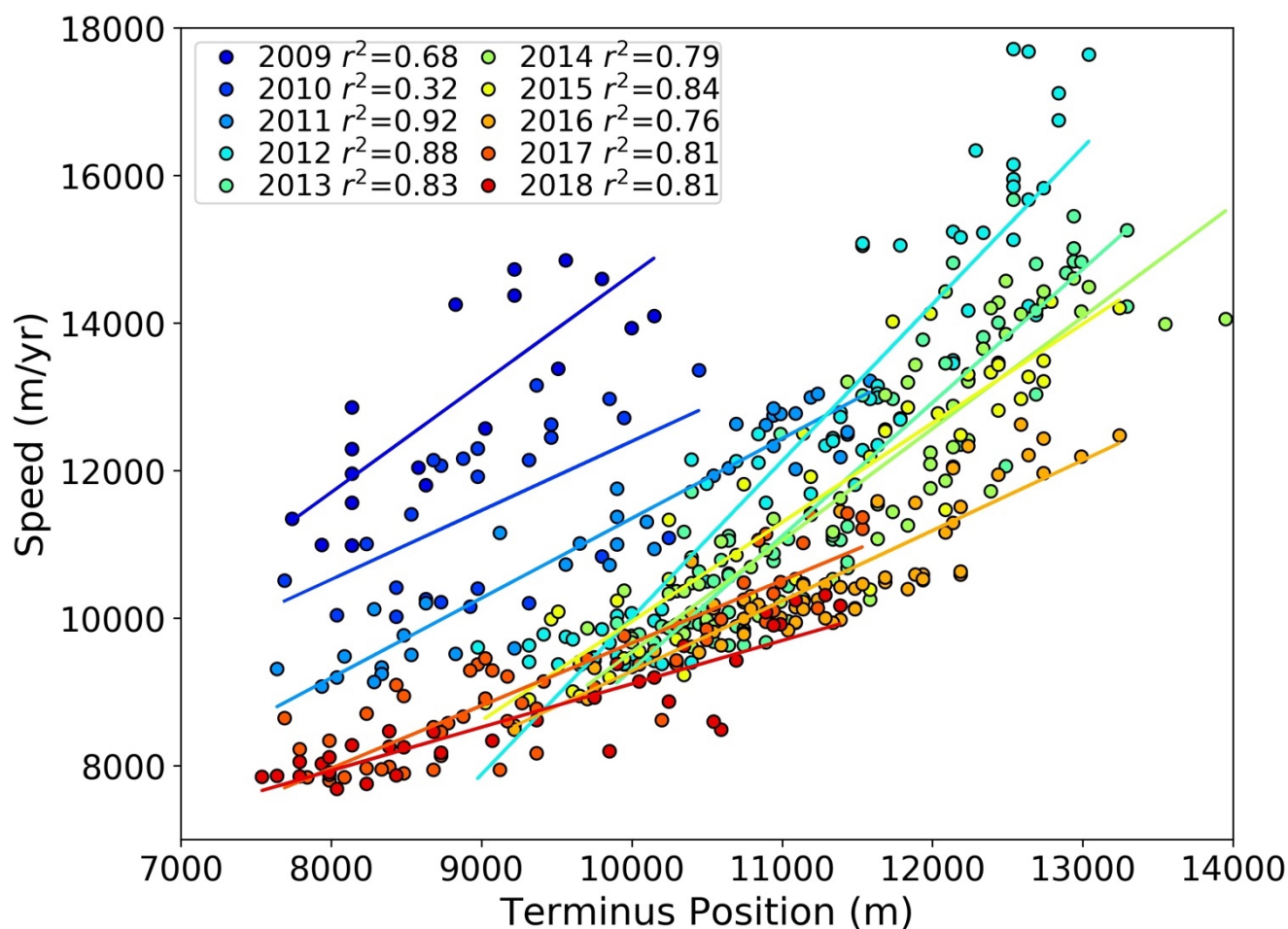
Figure 5. Speed at T_{max} -1 km (see grey points Fig. 1) as function of terminus position for each year from 2009 to 2018, with greater terminus positions indicating greater retreat. Lines show linear regressions for each year with r^2 values included in the legend.
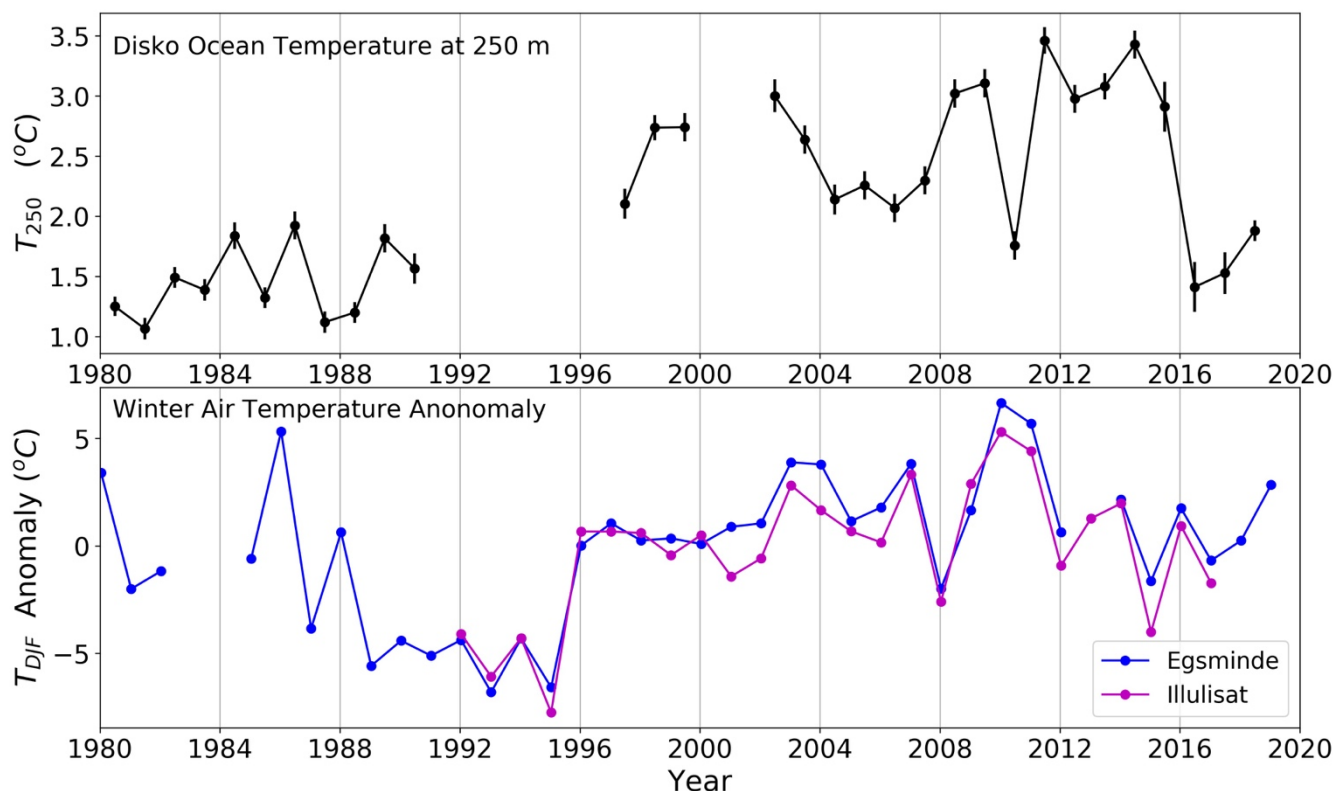
Figure 6. (top) Ocean temperatures at 250 m depth in Disko bay (all available casts for: -68.6º < latitude < 69.4º, -54º < longitude <
52º), which is based on a similar figure by Khazendar et al. (2019). Small differences exist based on the sampling region and
averaging scheme. The ocean temperatures for 2015-2018 are extracted from the Ocean Melting Greenland data set
(https://doi.org/10.5067/OMGEV-AXCTD) and the International Council for the Exploration of the Sea Oceanography
(http://www.ices.dk/marine-data/data-portals/Pages/ocean.aspx). To obtain estimates representative of 250 m depth, we averaged
temperatures from 225 to 275 m depth. The bars indicate uncertainty in the mean based on the number of points in the sampling
region. We take the mean intra-annual standard deviation averaged over the full record as the intrinsic uncertainty for a single
point (i.e., how representative a point measurement is for the entire region). We then scale this value by 1/sqrt(number of points) to
determine the plotted bar for each annual mean. (bottom) Winter 2-m air temperature (D-J-F) anomalies from weather stations in
Egsminde and Illulisat (GISTEMP Team 2019, 2019).

655

660

665
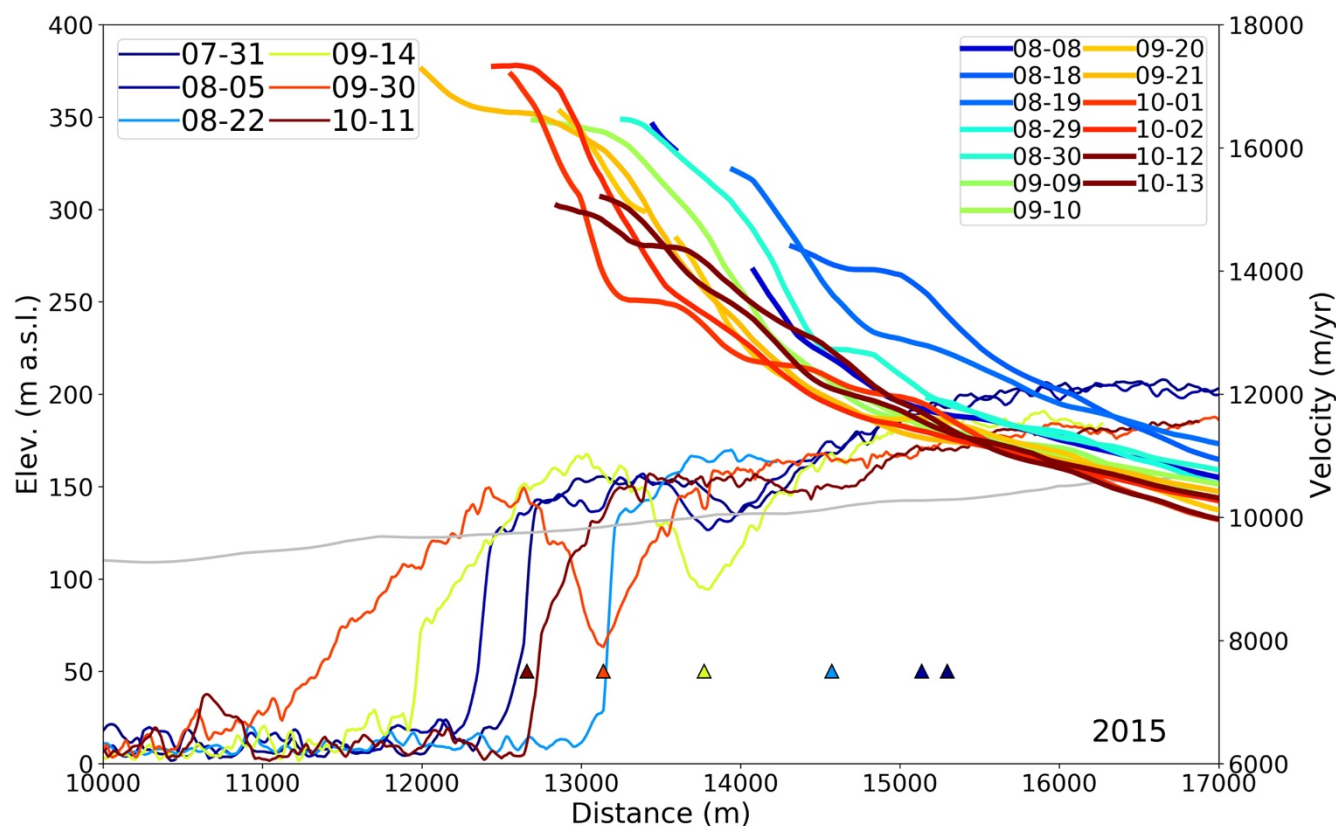
Figure 7. Elevation and velocity profiles for summer 2015 illustrating evolution of advecting transverse surface depressions. The legends give the nominal dates (MM-DD) in 2015. As in Fig. 3, grey line indicates nominal height of flotation. The triangles show the estimated locations (see text) of parcel of ice that evolved to form the bottom of the depression (see also white circles in Fig. 8) that served as a detachment point for a calving event(s) that occurred between September 30 and October 11.
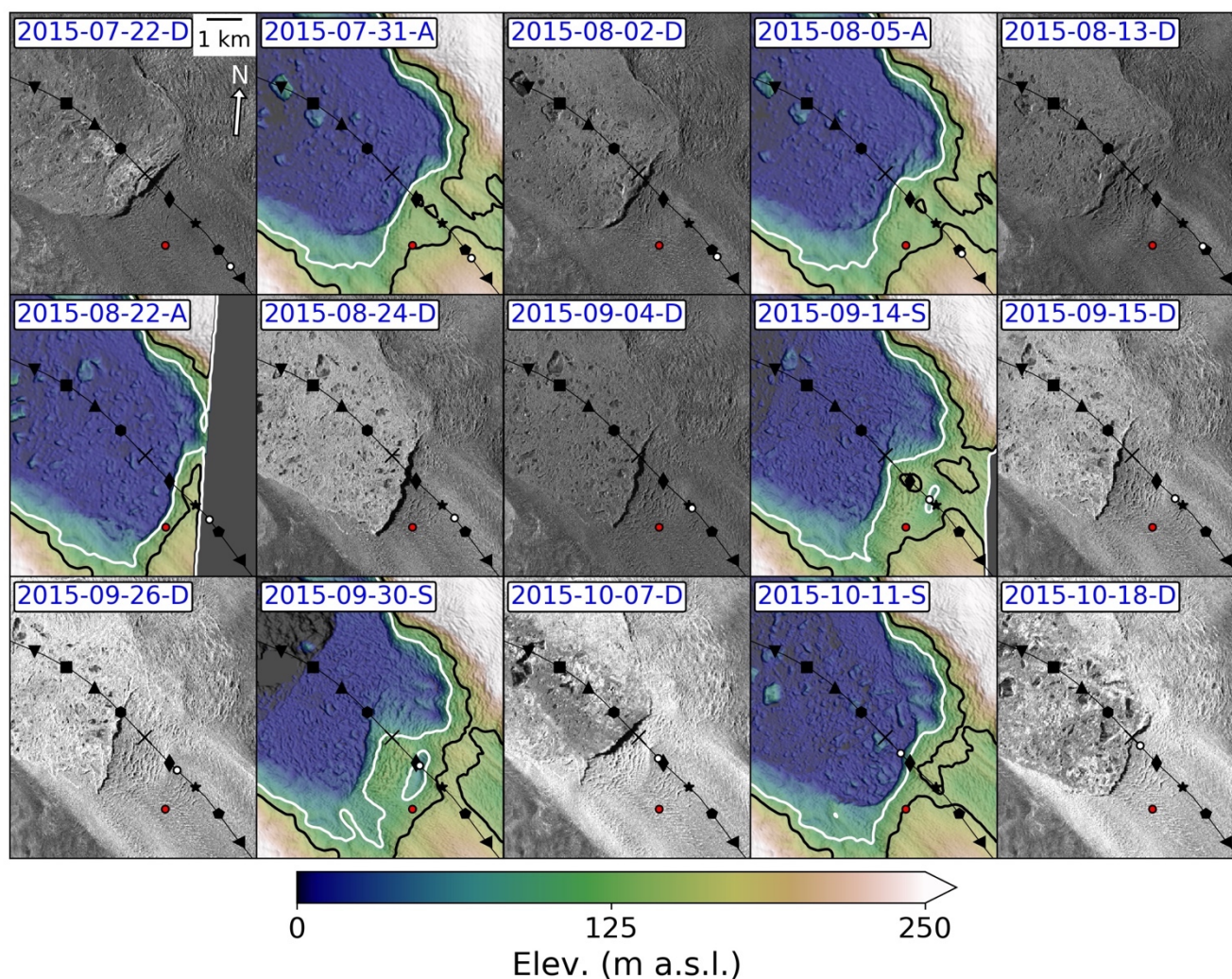
Figure 8. Time series of TerraSAR-X SAR backscatter imagery and colour shaded relief maps for late summer 2015 identified by date of acquisition (YYYY-MM-DD). The source of the data in each map is indicated by the letter after each date (D: TerraSAR-X images copyright DLR 2015, A: ASP World View, S: SETSM World View). The artificial illumination source for the DEM shaded surfaces was chosen to approximate the illumination angle of the TerraSAR-X radar. Note that the terminus in the radar imagery casts a true shadow, while the corresponding shadows in the shaded relief maps are based on the local slope/aspect. The red circle shows the location of M6, while the white circle tracks the parcel of ice that evolved to form the depression (e.g. September 30) described in the text (see also triangles Fig. 7).